



# Thermal methane pyrolysis in tubular quartz reactor: effect of temperature and surface-to-volume ratio on carbon yields and morphology

Emmanuel Busillo<sup>a</sup>, Andrea Nobili<sup>b</sup>, Clarissa Giudici<sup>c</sup>, Maria Paola Bracciale<sup>a</sup>,  
Alberto Cuoci<sup>c</sup>, Paolo De Filippis<sup>a</sup>, Martina Damizia<sup>a</sup>, Benedetta de Caprariis<sup>a,\*</sup>,  
Matteo Pelucchi<sup>c</sup>

<sup>a</sup> Department of Chemical Engineering, Materials and Environment, Sapienza University of Rome, Via Eudossiana 18, Roma, 00184, Italy

<sup>b</sup> Department of Mechanical Engineering, Stanford University, Stanford, 94305, CA, USA

<sup>c</sup> CRECK Modeling Lab, Department of Chemistry, Materials, and Chemical Engineering "Giulio Natta", Politecnico di Milano, Piazza Leonardo da Vinci 32, Milano, 20133, Italy

## ABSTRACT

This study provides an integrated experimental–modeling assessment of surface and gas-phase carbon formation in methane pyrolysis. Methane pyrolysis was experimentally investigated in a tubular flow reactor under atmospheric pressure to assess the effects of temperature and surface-to-volume (S/V) ratio on gas-phase chemistry, carbon yield and morphology. Two reactor configurations were examined: an empty tube ( $S/V = 4 \text{ cm}^{-1}$ ) and a tube packed with ceramic spheres ( $S/V = 10.7 \text{ cm}^{-1}$ ), with temperatures ranging from 950 to 1150 °C and deposition times from 30 min to 3 h. Major gas-phase hydrocarbon products were quantified via mass spectrometry, while solid carbon was recovered from hot surfaces for morphological and structural characterization by SEM and Raman spectroscopy. Results showed that temperature significantly increases solid carbon yield, reaching up to 60 wt% at 1150 °C. Morphological analyses revealed a transition from amorphous thin films to structured layers, shaped by deposition time, temperature and gas-phase evolution. Embedded carbon nanoparticles served as nucleation centers for cone-like growth, indicating a tight coupling between homogeneous and heterogeneous processes. Kinetic simulations using the CRECK model, which incorporates gas-phase chemistry for methane pyrolysis coupled with detailed soot and surface deposition mechanisms, reproduced key experimental trends and highlighted the role of  $\text{C}_2$  species and PAHs in triggering carbon nucleation and deposition. These results underscore the potential of thermal methane pyrolysis for  $\text{CO}_2$ -free hydrogen production, with tuneable carbon coproducts tailored for advanced material applications.

## 1. Introduction

In recent years, advancements in the production of carbon materials have driven developments in various industries, from energy to aeronautics and healthcare [1–3]. The properties, structure, and morphology of carbon materials can vary widely depending on the targeted market segment. Carbon materials with different morphologies can be deliberately synthesized through controlled decomposition pathways, enabling tailored production of specific carbon structures.

Among carbon materials, carbon black has the broader market. It is the industrial form of paracrystalline carbon with near spherical shape and high surface-area-to-volume ratio and is widely used as filler in elastomers, plastics and paints due to the capability of modifying the properties of the overall material in which it is dispersed [4]. Recent studies on methane pyrolysis demonstrate the critical influence of temperature on carbon morphology: at 850 °C, carbon particles reach sizes of approximately 2000 nm in carbon black form, while at 1150 °C

the particle size reduces to ~100 nm [5]. Shirsath et al. [6] reported carbon particle sizes in the range from 20 to 80 nm, with particle size decreasing significantly as the temperature increases from roughly 1073 K–1473 K, highlighting the temperature-dependent dynamics of carbon formation and growth.

Carbon nanotubes (CNT) are widely spreading in batteries, car parts, electronics and other goods. Their market is projected to amount to some 15.02 billion U.S. dollars in 2026 [7]. Pyrolytic carbon (PyC) is a nanocrystalline graphitic material which can be formed through hydrocarbons precursors decomposition and subsequent deposition on surfaces. Thanks to their thermal and mechanical properties pyrolytic carbons have been used in coating for pebbles in pebble bed reactors, rocket nozzles, heart valve coatings and other prosthetics [8]. All the above materials can be synthesized from thermal, catalytic or non-catalytic cracking of hydrocarbon precursors, through a complex network of reactions, comprising homogeneous gas-phase, including carbon particles nucleation and heterogeneous deposition or catalytic

\* Corresponding author.

E-mail address: [benedetta.decaprariis@uniroma1.it](mailto:benedetta.decaprariis@uniroma1.it) (B. de Caprariis).

<https://doi.org/10.1016/j.carbon.2025.121153>

Received 6 October 2025; Received in revised form 26 November 2025; Accepted 10 December 2025

Available online 13 December 2025

0008-6223/© 2025 The Authors. Published by Elsevier Ltd. This is an open access article under the CC BY license (<http://creativecommons.org/licenses/by/4.0/>).

growth reactions. The raising interest in hydrogen production to satisfy the projected increasing demand [9], endorses methane pyrolysis as an effective way to produce hydrogen while fixating the carbon content in valuable materials, without direct CO<sub>2</sub> emissions. Going in this direction, industrial research efforts in methane pyrolysis have demonstrated promising potential for hydrogen production. BASF's test facility at Ludwigshafen (operational since 2021) is investigating moving carbon bed reactor designs with target commercial deployment before 2030 [10]. Monolith Materials operates a commercial facility in Nebraska achieving hydrogen production of approximately 5 kilotonnes per annum and carbon black production of approximately 14–15 kilotonnes per annum at full commercial scale (TRL 9), with demonstrated performance from over 3700 operating hours at demonstration scale [11]. Such industrial progress complements academic research by addressing practical scale-up challenges and accelerating the transition toward sustainable hydrogen production [12].

While this process can be represented by the global endothermic reaction  $\text{CH}_4(\text{g}) = \text{C}(\text{s}) + 2\text{H}_2$ , which establishes the well-defined thermodynamic limit of 25 wt% hydrogen and 75 wt% solid carbon production, the primary challenge lies in controlling the complex chemical kinetics that dictate carbon morphology and process efficiency [13]. Unlike steam methane reforming, producing more than 10 tons of CO<sub>2</sub>-equivalent per ton of hydrogen produced [14], methane pyrolysis generates no carbon dioxide as a direct reaction product. Its overall emissions, however, depends on supplying renewable or low-carbon heat to drive this endothermic process enabling very low CO<sub>2</sub> intensity when powered by renewable sources. Process efficiency and control of carbon morphology remain critical, as they influence energy demand, carbon valorization potential, and the resulting life-cycle CO<sub>2</sub> footprint. Carbon materials can be produced in cracking reactors (e.g. plug flow reactor) operating at high temperatures ( $T > 800^\circ\text{C}$  [12]), in the form of carbon nanoparticles and pyrocarbon at the reactor walls. As widely understood from many other high-temperature industrial pyrolysis processes (e.g. steam cracking), wall deposition may be undesired as it affects reactor performances (product yields) [15,16]. The competition between gas-phase nucleation and surface reactions controls whether carbon forms as suspended particles or wall deposits, a balance strongly influenced by reactor geometry and residence time. In the early reactor stages and at moderate temperatures (850–1000 °C), surface reactions dominate, with carbon deposition rates controlled by the availability of active surface sites and the concentration of adsorbed hydrocarbon intermediates. At higher temperatures ( $\geq 1150^\circ\text{C}$ ), however, the rapid gas-phase reaction rates lead to near-complete methane conversion at the reactor inlet, causing a transition from mass-transfer-limited to kinetically limited regimes where gas-phase homogeneous nucleation becomes increasingly competitive with surface deposition [17].

Deposition kinetics models that explicitly couple surface reaction mechanisms with gas-phase chemistry effectively predict carbon deposition rates from hydrocarbon precursors, with surface species and elementary reactions accounting for complex pathways involving intermediate carbon-containing molecules. In tubular flow reactor studies combining kinetic modeling with experiments over wide temperature ranges (1273–1873 K) and coupling gas-phase mechanisms with surface deposition models shows that hydrogen addition strongly influences methane conversion and suppresses unwanted hydrocarbon byproducts [18]. At optimal conditions (1673 K with  $\text{H}_2:\text{CH}_4 = 2$ ), solid carbon yield reaches 84 % with gaseous byproducts remaining below 1 mol%, demonstrating the feasibility of near-complete separation of hydrogen and carbon products. Carbon deposition is highly non-uniform along the reactor: maximum deposition rates occur immediately downstream of the reactor entrance (hot zone inlet), where C<sub>2</sub> intermediates and aromatics are most abundant; with increasing residence time, the total amount of deposited carbon increases significantly, indicating continued carbon formation and surface accumulation throughout the reactor volume.

In authors' previous work methane pyrolysis in a quartz flow reactor ( $T = 875\text{--}975^\circ\text{C}$ ,  $P = 1\text{ atm}$ ) was investigated characterizing solid product morphology as well as gas-phase intermediates and products [19]. The CRECK kinetic model [20–22] was used to interpret experimental observations by gas-phase chemical kinetics analysis. This study extends the analysis by investigating the effects of temperature, deposition time and surface-to-volume ratio on gas-phase composition, carbon nanoparticles and carbon deposits formation.

A key but underexplored aspect of carbon formation kinetics is the distinction between carbon deposits on reactor surfaces and gas-phase nanoparticles, particularly regarding how particle deposition mechanisms shape material morphology and structural properties. Although homogeneous carbon formation during hydrocarbon thermal decomposition is well-known, the differential accumulation and structural evolution of carbon deposits on reactor surfaces versus suspended nanoparticles remain largely unexplored.

This work provides the first systematic characterization of the interplay between carbon particle deposition and surface carbon accumulation, integrating kinetic modeling and carbon morphological analysis via scanning electron microscopy and Raman spectroscopy to elucidate carbon formation on surfaces under relevant conditions. For the first time, the two distinct carbon typologies, deposited and homogeneous, were simultaneously measured and characterized, enabling the determination of averaged carbon deposition and homogeneous nucleation rates and their comparison with model predictions. This combined approach clarifies how operating variables govern carbon distribution and microstructural features, offering new insights for potential carbon valorization.

The experiments were conducted in a quartz tubular reactor, with ceramic spheres inserted into the quartz tube to increase the surface-to-volume ratio. Temperature varied between  $T = 950\text{--}1150^\circ\text{C}$ , a range of interest for current thermal cracking applications [23]. Carbon deposits were collected from the reactor walls, while soot was trapped at the end of the reactor using quartz wool. The carbon deposits were quantified and characterized from different reactor zones to assess the effect of varying gas-phase compositions on the morphology of the deposited carbon. Simulation results obtained with the CRECK kinetic model describing gas-phase pyrolysis [22,24], carbon nanoparticles formation through a discrete sectional method [20,22] as well as carbon deposition on the surface as described in Serse et al. [25] are compared with experimental measurements of gas-phase intermediates as well as surface carbon and carbon nanoparticles formation, providing mechanistic insights on the impact of gas-phase dynamics on observed morphological features.

## 2. Materials and methods

### 2.1. Experimental methods

The experimental tests were conducted in a tubular quartz flow reactor (i.d. = 1 cm) coiled inside an alumina tube. The reactor was placed in an electric oven operating at  $T = 950\text{--}1150^\circ\text{C}$  (Fig. 1) with a heated length of 20 cm. The oven temperature is continuously controlled by a K-type thermocouple. Pure methane ( $\text{CH}_4 > 99.9\%$  vol) has been injected (SOL Group, UN 1971) into the system at constant flow rate for each test controlled by Brooks Instrument flowmeter.

C<sub>2</sub> gas products composition (C<sub>2</sub>H<sub>6</sub>, C<sub>2</sub>H<sub>4</sub> and C<sub>2</sub>H<sub>2</sub>) at the outlet of the reactor have been measured by quantitative mass spectrometry (QGA Hiden). Mass spectrometry was selected for its real-time analysis, high sensitivity, and fast response time, enabling continuous monitoring without chromatographic separation delays. The mass spectrometer was previously calibrated using a specific calibration cylinder containing a known composition of target species, i.e., C<sub>2</sub>H<sub>6</sub> = 0.489 mol%, C<sub>2</sub>H<sub>4</sub> = 1.010 mol%, C<sub>2</sub>H<sub>2</sub> = 0.502 mol% (SIAD S.p.A.). At the end of each experimental tests, the reactor has been cooled with Argon (SOL Group, UN 1006). All experiments were performed in triplicate to ensure data

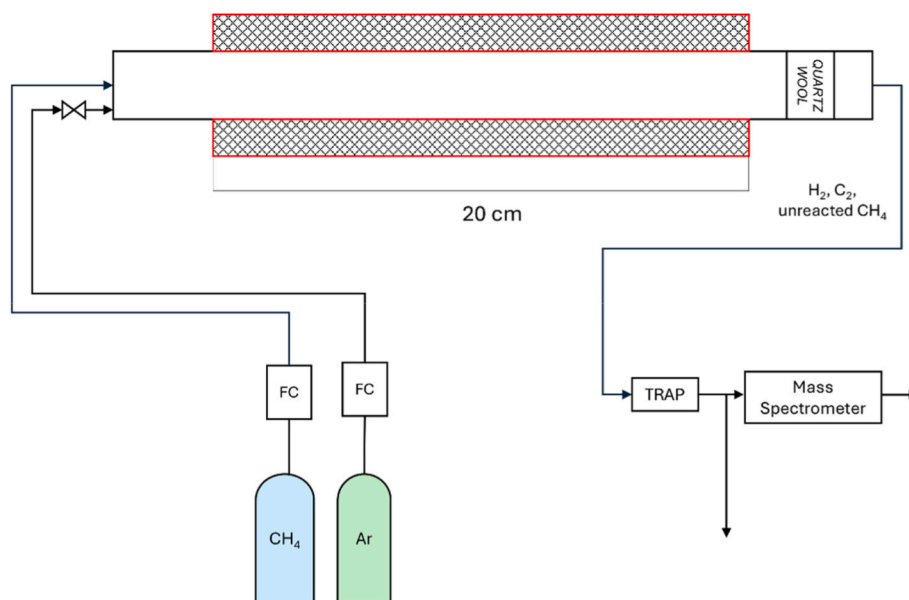


Fig. 1. Schematic representation of the experimental set-up adopted in this work.

reliability and to allow for an accurate assessment of experimental error.

The surface-to-volume ratio (S/V) critically influences methane pyrolysis by increasing the available active surface for heterogeneous carbon deposition reactions, which predominantly affect the initial stages of the process, while at longer times and higher temperatures, homogeneous gas-phase reactions become the main controlling mechanism [26]. To investigate the effect of the surface-to-volume ratio (S/V) on carbon deposition, two configurations were adopted (Fig. 2). The first one (Fig. 2A) consisted of an empty tubular quartz reactor, with an overall S/V ratio of  $4\text{ cm}^{-1}$ , calculated based on the reactor dimensions as  $S/V = 4/D$ . To increase the surface area exposed to the reaction, the second configuration (Fig. 2B) consisted of filling the same reactor with ceramic spheres (composition in wt%: O: 42.32; Al: 14.96; Si: 37.19), each having a diameter of  $6 \pm 0.1\text{ mm}$ . The EDS spectrum and SEM images of the ceramic spheres utilized in this study are presented in the Supplementary Material (Fig. S1). In this case, the S/V ratio was

determined as the ratio between the surface area exposed to gas species and the free volume available to the gas, resulting in an S/V of  $10.7\text{ cm}^{-1}$ . Although adding spheres changes flow dynamics by inducing turbulence and affecting surface phenomena, this configuration was selected to increase the surface-to-volume ratio without excessively reducing the reactor diameter, which would be impractical due to rapid clogging from carbon deposition. Both configurations included a quartz wool trap positioned at the reactor outlet, in the cold zone, to collect carbon nanoparticles produced in the gas phase. In the first configuration, carbon deposits were collected on the reactor walls, and two collection zones were identified (Zones A1 and A2 in Fig. 2). Zone identification was based on practical considerations to ensure clean carbon sample collection from reactor walls. Since carbon samples collected from the walls were obtained mechanically, zone demarcation prevented cross-contamination between different deposit locations.

In the second configuration, carbon deposits were collected on the

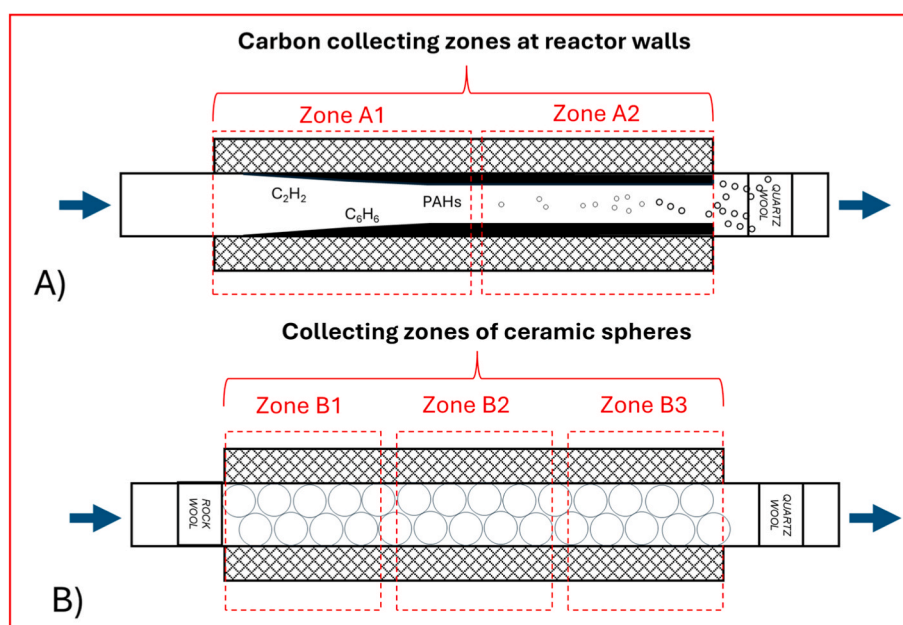


Fig. 2. Reactor configurations: A) void reactor; B) packed with ceramic spheres.

surfaces of the ceramic spheres, and three collection zones were considered (Zones B1, B2 and B3 in Fig. 2). The presence of packing material with surfaces at fixed positions, where spheres are arranged sequentially along the reactor axis, prevented cross-contamination between regions and enabled distinct collection of carbon in three separate zones. This procedure enables the collection of carbon formed under different gas-phase compositions as a function of the residence time in the different zones and enables the assessment of the influence of homogeneous chemistry on the morphology and thicknesses of the carbon deposits. Reaction times, defined as the duration available for carbon deposition ( $t_D$ ), were varied from 30 min to 3 h to determine the deposition rate by measuring the mass and the thickness of the carbon deposits. Varying test duration also enabled the evaluation of the effect of deposition time on the morphology of the carbon collected from the same sampling positions.

The initial methane flow rate was fixed in void reactor (Fig. 2A) to  $\dot{V}_1 = 25$  nml/min. To fairly compare the results from the two configurations, a correction to the initial methane flow rate was applied for the tests with ceramic spheres to maintain the gas residence time constant at the inlet conditions: therefore, the initial methane flow rate was reduced to  $\dot{V}_2 = 16.9$  nml/min in the case of ceramic spheres to account for the reduction in gas volume available for the reaction ( $V_2 = V_1 - N(4/3\pi R^3)$ , where  $V_2$  is the available to the gas volume with the spheres,  $V_1$  is the total volume of the heated zone, and  $N$  and  $R$  are the number of ceramic spheres ( $N = 45$ ) and their average radius ( $R = 3$  mm), respectively.

To quantify the two types of produced carbon (i.e. carbon nanoparticles and deposited pyrolytic carbon) the following procedure was applied. In both configurations, the reactor equipped with the quartz trap was weighed before and after the tests to determine the total amount of carbon produced ( $C_{TOT}$ ). The quartz wool trap was then removed, and the reactor weighed once again to obtain the value of the deposited carbon ( $C_D$ ). The mass of carbon nanoparticles trapped in the quartz wool ( $C_{TRAP}$ ) was then determined by difference as:

$$C_{TRAP} = C_{TOT} - C_D \quad (2)$$

The carbon products have been characterized by Scanning Electron Microscopy (SEM) and Raman spectroscopy. SEM images were acquired using a High Resolution-Field Emission Scanning Electron Microscope (HR-FESEM, AURIGA Zeiss). Raman spectra were recorded at room temperature with a SENTERRA micro-Raman dispersive spectrometer (Bruker Optics), using a CW diode-pumped solid-state laser with a wavelength of 532 nm and a 20 $\times$  objective (Olympus B41). The spectra were obtained with a laser power of 5 mW, 50 coadditions, and an integration time of 1 s, within the spectral range from 500 to 4000  $\text{cm}^{-1}$ . The  $I_D/I_G$  ratio, indicating the level of carbon ordering, was determined from the total intensities of the D and G bands. To resolve all relevant Raman contributions, the experimental spectra were deconvoluted into Gauss-Lorentzian components following baseline subtraction, using OPUS 8.0 software (Bruker Optik GmbH) and applying the Levenberg-Marquardt fitting algorithm. The quality of the fit was assessed by ensuring a residual Root Mean Square (RMS) error below 1 % of the data range.

## 2.2. Modelling methods

The CRECK kinetic model consists of i) a gas-phase subset [22,27] describing pyrolysis chemistry of methane and higher molecular weight hydrocarbons, including mono- (MAHs) and polycyclic aromatic hydrocarbons (PAHs) up to 4-rings ( $C_{16}H_{10}$ ), ii) a soot formation mechanism describing carbon nanoparticles and aggregates as in Nobili et al. [20], and iii) a surface deposition mechanism presented in Serse et al. [25]. The soot model consists of 25 discrete sections, named BINs. BIN1-4 represent large PAHs with more than 20C atoms up to 160 C-atoms. The smallest soot particle is BIN5, with  $D_p \sim 2$  nm and 320C atoms. Particles up to BIN12 ( $D_p \sim 10$  nm, 40000 C-atoms) are assumed

to be spherical, while BIN13–25 are regarded as aggregates (up to  $D_p \sim 1$   $\mu\text{m}$ ,  $3 \cdot 10^8$  C atoms with fixed fractal dimension of 1.8 [20]). A detailed description of the CRECK soot sectional model can be found in previous works [20,24,28,29]. Overall, the gas-phase and soot mechanisms comprise 372 species and 719 reactions. The solid carbon deposition mechanism presented by Serse et al. [25] is based on [30] and involves 66 surface species and 275 reactions. 131 elementary steps describe the reactivity of armchair sites, whereas the remaining 144 describe zigzag sites. Based on the assumption of a fast formation of a carbon layer [31] on the reactor walls we assume graphite with a constant density of superficial sites ( $8 \cdot 10^{14}$  sites/ $\text{cm}^2$ ) as the deposition surface. Reaction classes considered in the pyrocarbon deposition mechanisms have been discussed in Refs. [25,30].

As in our previous work [19], the reactor was modeled as heterogeneous 1D plug-flow reactor ( $L_{\text{heat}} = 20$  cm,  $D = 1$  cm) implemented in the OpenSMOKE++ framework [32]. Conservation equations used to describe the reactor have been previously described in Ref. [25]. The S/V parameter is given as input during simulations to define the available surface for heterogeneous processes to occur and we assumed that 50 % of surface sites were armchair like and 50 % zig-zag like, in accordance to previous works where deposition rates were found to minorly depend on such parameter [30].

## 3. Results and analysis

### 3.1. Experimental results

Experiments and model simulations for methane conversion and hydrogen production under similar operating conditions were presented and discussed in our previous work [19]. The outlet hydrogen content strongly depends on temperature, with hydrogen mole fractions across both reactor configurations increasing from  $\sim 10$  % at 950  $^\circ\text{C}$  to  $\sim 89$  % at 1150  $^\circ\text{C}$  (Fig. S2), highlighting the marked enhancement in hydrogen production at elevated temperatures. The yield of  $C_2$  intermediates, calculated as the ratio of moles of  $C_2$  products formed to moles of methane consumed, varies between 2 % and 11 %, and is shown as a function of temperature and reactor configuration in Fig. S3. Fig. 3 shows the mole fractions of the measured gas-phase  $C_2$  intermediates as a function of temperature in the case of void reactor ( $S/V = 4$   $\text{cm}^{-1}$ ) and of the packed reactor ( $S/V = 10^{-7}$   $\text{cm}^{-1}$ ).

Peak mole fractions of both ethylene and ethane are observed both in the case of packed bed and of the empty reactor at  $T = 1000$   $^\circ\text{C}$ . Acetylene plays a major role in surface deposition as well as PAHs growth through the HACA mechanism [33]. Peak mole fraction of acetylene is obtained also at  $T = 1000$   $^\circ\text{C}$  in the void reactor, which is characterized by a lower surface area. Lower mole fractions of  $C_2H_2$  and  $C_2H_4$  are instead measured in the packed reactor, primarily due to heterogeneous surface growth reactions.

Fig. 4 shows experimental results concerning the solid carbon products as a function of temperature in the case of void reactor ( $S/V = 4$   $\text{cm}^{-1}$ ) and of the packed reactor ( $S/V = 10^{-7}$   $\text{cm}^{-1}$ ). With respect to the theoretical limit of 75 % wt. of carbon products, at the highest temperature condition ( $T = 1150$   $^\circ\text{C}$ ) of the present experiments yields up to 60 % of solid carbon have been obtained. Total carbon mass produced ( $C_{TOT}$ ) increases for higher temperatures as reported in Fig. 4a. The higher amount of carbon products in the case of void reactor is due to higher deposition time for the void configuration test (60 min) if compared to the packed bed configuration (30 min). The different deposition times were employed to maintain continuous operation in each reactor type while avoiding carbon accumulation that could bias gas measurements and compromise data quality. To address potential time-dependent effects and ensure meaningful comparison between reactor configurations, carbon yields are normalized by time, isolating the effects of variables such as temperature and surface-to-volume ratio. This time-normalized analysis approach averages potential time-related influences on the results, allowing fair attribution of observed



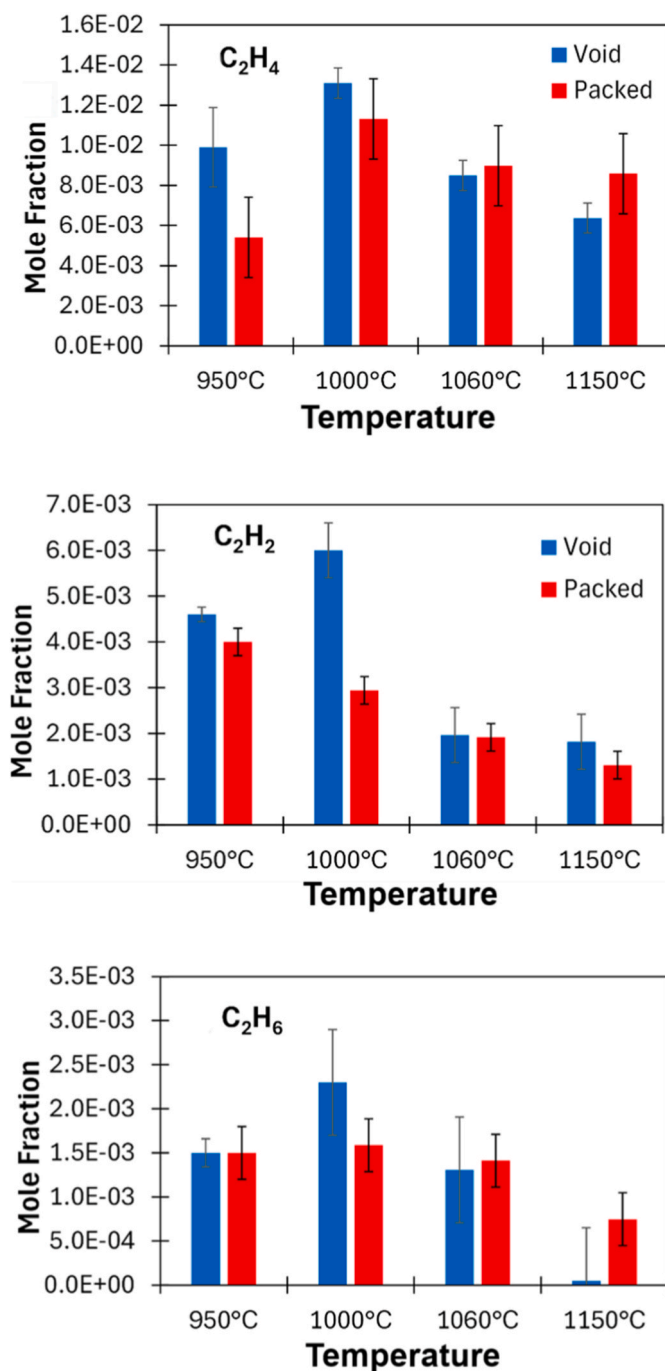


**Fig. 3.**  $C_2$  species mole fractions as a function of temperature.  $T = 950$ – $1150$  °C,  $S/V = 4$   $cm^{-1}$  (void reactor, blue,  $t_D = 60$  min) and  $10.7$   $cm^{-1}$  (packed reactor, red,  $t_D = 30$  min). (For interpretation of the references to colour in this figure legend, the reader is referred to the Web version of this article.)

differences to the actual variables of interest rather than experimental duration. In both systems, rapid transients occur only during initial surface coverage; after steady state is reached, carbon formation and gas production rates remain nearly constant, as evidenced by stable conversion and product composition values throughout the experiments (Fig. S4). The higher availability of deposition surface in the packed bed reactor motivates the higher carbon conversion rates observed in Fig. 4b compared to the void setup. As summarized in Fig. 4c, the amount of deposited carbon ( $C_D$ ) increases linearly with temperature in both the void and packed reactor. Although carbon nanoparticle ( $C_{TRAP}$ )

production also exhibits temperature-dependent enhancement in both configurations (Fig. 4d), the trend is hidden by temperature-dependent carbon nanoparticle losses, wherein elevated temperatures promote volatilization processes that compromise the experimental carbon mass balance. Experimental results for both the gas-phase measurements and the carbon products quantification are provided in tabular form in the Supplementary Material (Tab. S1, S2 and S3).

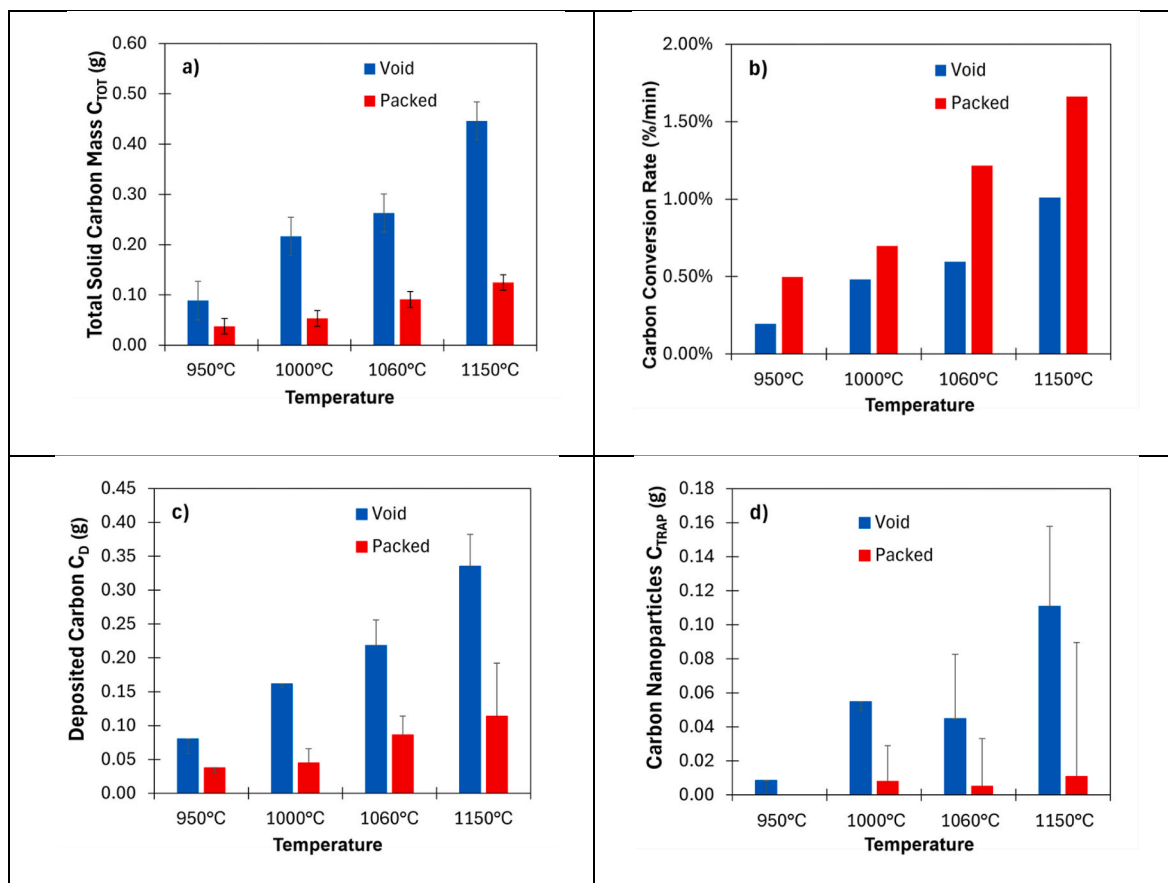
### 3.1.1. Characterization of the carbon products from the void reactor configuration ( $S/V = 4$ $cm^{-1}$ )

SEM analysis can be employed to examine the cross-section of a film, enabling the determination of film thickness, the calculation of film growth rates, and the investigation of growth mechanisms [34]. As expected, SEM images revealed a different morphology between the carbon produced at  $T = 950$ – $1000$  °C found at reactor walls (Fig. 5, a) and those trapped in the quartz wool (Fig. 5, b). The carbon trapped in the quartz wool consists of particles nucleated in the gas phase whose shape could be linked to the isotropic deposition of chemical species around nuclei and surface energy minimization issues. These particles appear to be very similar to black carbon particles reported in Ref. [15], whose particle size distribution function (Fig. 6) is obtained from Fig. 5b. The mean diameter of the 50 random particles highlighted in Fig. 6 by ImageJ analysis resulted to be of 490 nm.

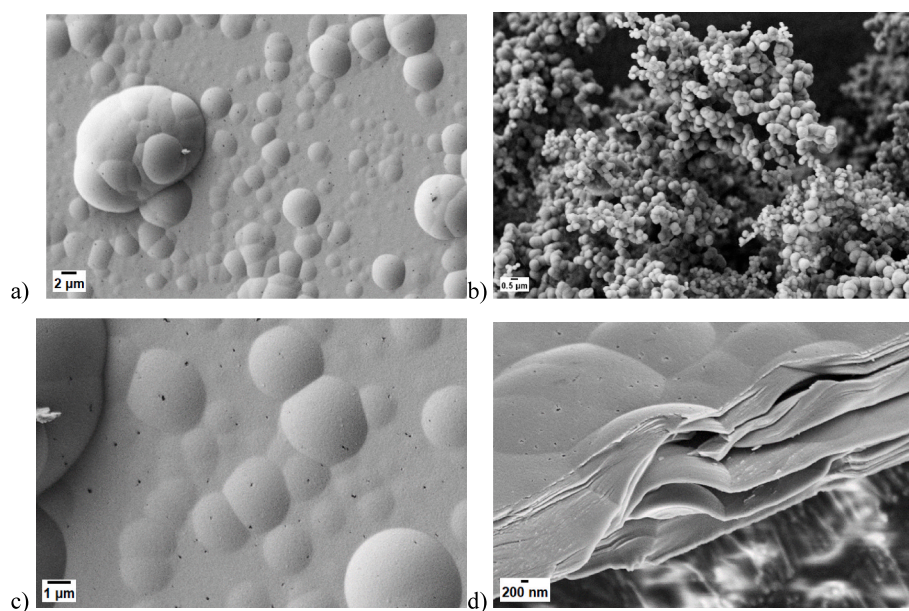
The carbon collected at reactor walls (Fig. 5a–c, d) produced at  $1000$  °C appears to be very similar to pyrolytic carbon found in other similar studies [35]. Its morphology is specifically influenced by the presence of surface defects, deposition time, gas phase composition and by the maturation of carbon particles which may evolve in the gas-phase exiting the reactor or nucleate on the reactor walls. Fig. 5a and c show a continuous carbon film with the presence of several nodules, which are supposed to grow with successive deposition reactions, transmitting the information on surface asperity and/or additional defects up to the surface of carbon deposit [36]. The formation of uniform carbon film is expected to arise from the merging of specific carbon islands initially nucleated on the substrate through different mechanisms including random nucleation of isolated islands, nucleation at local surface defects and secondary nucleation, i.e. nucleation at the edges of pre-existing carbon islands [37]. The specific physico-chemical properties of such carbon islands and the detailed nucleation process remain unclear. However, according to some authors, for carbon deposition at atmospheric pressure and long residence times, the deposition process may involve the formation of a transient liquid organic phase. This phase, which is pitch-like and rich in polyaromatic hydrocarbons (PAHs) and other smaller molecules, undergoes transformation into solid carbon through a progressing carbonization process [38].

Fig. 5c and d highlight the presence of pores on pyrolytic carbon surface. Pore dimensions range between 50 and 200 nm. Reznik et al. hypothesized that such alteration in the pyrolytic structure is due to the dehydrogenation process, which is affected by the thermal treatment of the deposit after the termination of the deposition, e.g. by the reactor cooling rate [39]. Considering the cooling rate adopted in our work ( $5$ – $10$  °C/min), it is likely that hydrogen released from pyrolytic structure contributed to the formation of the pores depicted in Fig. 5c and d. Additional reasons for the observed porous structure may be PAHs desorption or bubbling phenomena of the transient liquid-like phase. The thermal treatment following the deposition of pyrolytic carbon can be tailored to influence the microstructure of various carbon-based materials formed from gaseous hydrocarbons, including pyrolytic matrices in carbon/carbon composites.

SEM images of carbon deposits at the two different locations (Fig. 2, Zone A1 and A2) are shown in Fig. 7. The morphology of carbon deposits is very different between carbons collected at the beginning and at the end of the heated zone. The carbon deposits collected at Zone A1 are relatively thin and consist of layered sheets. In contrast, at the end (Zone A2), the deposits exhibit hemispherical structures that significantly influence the overall roughness of the carbon deposits. The change in



**Fig. 4.** Experimental solid carbon products yield at  $T = 950\text{--}1150\text{ }^{\circ}\text{C}$ ,  $S/V = 4\text{ cm}^{-1}$  (void reactor, blue,  $t_D = 60\text{ min}$ ) and  $10.7\text{ cm}^{-1}$  (packed reactor, red,  $t_D = 30\text{ min}$ ). a) total solid carbon mass (g), b) carbon conversion rate, i.e. the percentage of carbon in the initial methane that is converted into solid carbon per unit time (%/min), c) deposited carbon mass (g), d) carbon nanoparticles mass from wool trap (g). Error bars indicate the carbon deficit required to close the carbon mass balance, representing the difference between expected and measured carbon production. (For interpretation of the references to colour in this figure legend, the reader is referred to the Web version of this article.)



**Fig. 5.** SEM images of carbons collected in methane pyrolysis tests ( $T = 950\text{--}1000\text{ }^{\circ}\text{C}$ ): a), c), d) at the centre of the reactor heated zone ( $T = 1000\text{ }^{\circ}\text{C}$ ); b) trapped in the quartz wool ( $T = 950\text{ }^{\circ}\text{C}$ ).

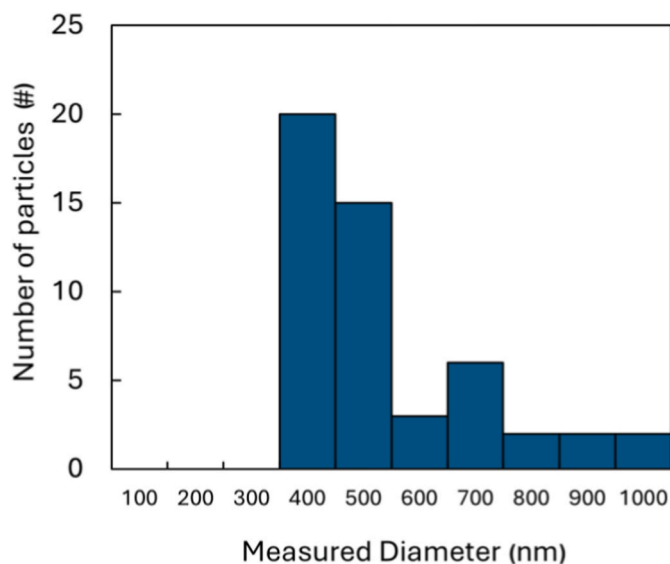


Fig. 6. Size distribution of carbon particles depicted in Fig. 5b.

morphology observed at the different positions is attributed to changes in deposition rates, with carbon particles nucleating and growing in the gas phase before depositing on the substrate [40].

These position-dependent morphological transitions are supported by foundational work on carbon deposition mechanisms, which established that the relationship between gas-phase particle formation and surface molecular deposition controls deposit microstructure. Our reactor position functions as a continuous CVD parameter, where axial variations in residence time and hydrocarbon conversion produce the same morphological evolution documented in classical CVD studies [40].

As described in the simplified scheme of the proposed mechanisms of carbon formation depicted in Fig. 8, the composition of the gas phase affects significantly the morphology of the carbon deposit. At low methane decomposition product concentrations, corresponding to collection zone A1 (low deposition rates), fewer and smaller particles

are formed, leading to primarily molecular deposition, with limited nucleation sites for new growth and with no evidence of embedded particles. The mean thickness of the carbon deposit measured in this case after 2 h of test (Fig. 7 a and c) is  $1.2 \pm 0.2 \mu\text{m}$ . At higher hydrocarbon concentrations (high deposition rates), more and larger gas-borne particles are formed and assimilated into the deposit layers, leading to altered growth structures with higher particle incorporation. In this case, the thickness of the layer varies depending on the surface, on the presence of carbon particles and their post-deposition growth, i.e. the continued accumulation and growth of already deposited particles through chemical reactions or particle aggregation. In Fig. 7 b and d, the thickness of the carbon deposit varies between  $5.8 \pm 0.6$  and  $7.1 \pm 0.2 \mu\text{m}$  when hemispherical cap of post-deposition growth is considered. As a result, following the maturation of the gas phase along the reactor, the thickness of the carbon deposits increases from Zone A1 to Zone A2, suggesting approximately a mean deposition growth rate of  $3.4\text{--}4.2 \mu\text{m/h}$ .

To summarize, the difference in morphological features could be explained by the different composition of the gas phase and the presence of carbon particles with specific dimensions, altering the direction of growth of carbon sheets and giving rise to the formation of cone-grown structures which are not related to the presence of surface defects, but only to the deposition of carbon nanoparticles nucleated in the gas-phase (Fig. 8). Fig. 9 show the profiles of the major  $\text{C}_2$  species (Fig. 9a), and aromatics and carbon nanoparticles (Fig. 9b) as a function of reactor length in the void reactor configuration obtained through model simulations, confirming the qualitative interpretation of the different morphological features at different locations inside the reactor of Fig. 8.

In particular, it is possible to observe that between 0 and 5 cm of reactor length, at limited conversions (i.e.  $<5\%$ ), only  $\text{C}_2$  intermediates are significantly available. Ethane ( $\text{C}_2\text{H}_6$ ) mole fraction rapidly increases in the early stage of the reactor due to methyl recombination, reaches a maximum at 10 cm, and then slightly decreases due to H-abstraction and dehydrogenation reactions (Fig. S5). Ethylene ( $\text{C}_2\text{H}_4$ ) dehydrogenation leads to the formation of acetylene that onsets the formation of first ring aromatics (e.g., benzene,  $\text{C}_6\text{H}_6$ ) at  $>5$  cm length. Molecular growth to larger aromatics (e.g., naphthalene,  $\text{C}_{10}\text{H}_8$ ) primarily follows through the HACA mechanism. Large PAHs with  $>100$  C-atoms finally nucleate to carbon nanoparticles after 10 cm length. Zone

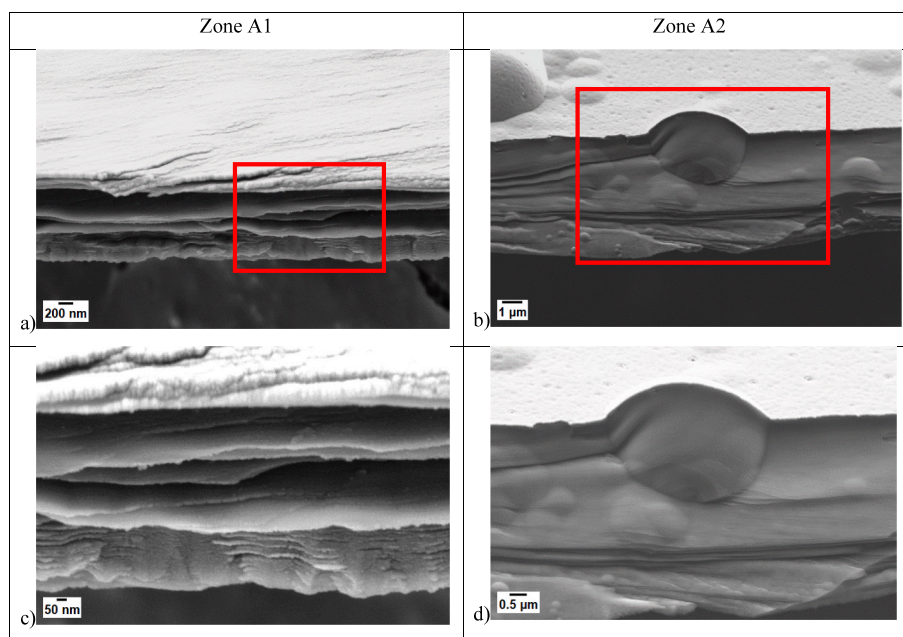


Fig. 7. SEM Images of carbon deposits collected at reactor walls at the zone A1 (a,c) and A2 (b,d) at  $1000^\circ\text{C}$ ,  $t_D = 120$  min. Areas within red rectangles in a) and c) are zoomed in c) and d), respectively. (For interpretation of the references to colour in this figure legend, the reader is referred to the Web version of this article.)



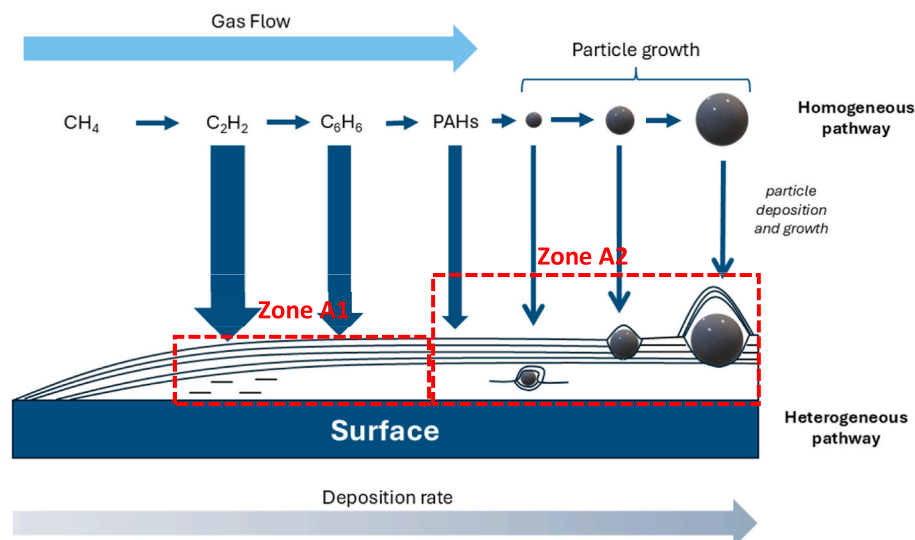


Fig. 8. Scheme of proposed mechanism with homogeneous and heterogeneous mechanisms of carbon formation.

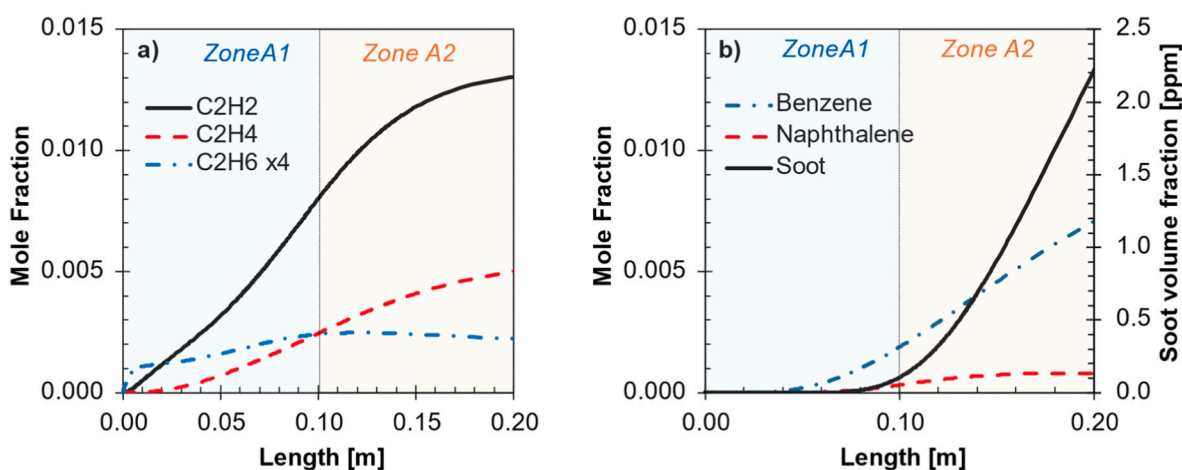


Fig. 9. Mole fraction profiles of a) major  $\text{C}_2$  gas-phase species and b) benzene, naphthalene and soot particles obtained from model simulations in a homogeneous flow reactor at  $T = 1000^\circ\text{C}$ . Zones A1 and A2 correspond to the experimental collection regions, associated with positions 0–10 cm and 10–20 cm along the reactor length in the simulation domain.

A1, where layered sheets are formed (Fig. 7a and c) can be qualitatively located where PAHs start to form, i.e. around 7–8 cm length, as from the  $\text{C}_{10}\text{H}_8$  profile (Fig. 9), until the inflection point in the aromatic species profiles ( $\sim 12$  cm) indicative of significant formation of carbon nanoparticles. In the last part of the reactor (Zone A2) hemispherical structures highlighted by the SEM analyses of Fig. 7 are formed due to particle growth in the gas-phase and nucleation at the reactor walls.

### 3.1.2. Characterization of the carbon products from the packed reactor configuration ( $S/V = 10.7\text{ cm}^{-1}$ )

SEM images of carbon deposits on ceramic spheres collected from three reactor zones (B1–B3,  $T = 1000^\circ\text{C}$ , see Fig. 2) are presented in Fig. 10. The reactor zone significantly influences carbon morphology. This effect is attributed to the corresponding gas-phase composition. In the initial zone, carbon deposits appear amorphous and non-uniform, forming in some areas a very thick carbon layer (Fig. 10, zone B1 and Fig. S6). In contrast, carbon collected from the middle zone shows a more ordered layer, with carbon particles approximately 500 nm in diameter embedded on its surface (Fig. 10, zone B2). It is therefore interesting to observe that these particles are dimensionally similar to the carbon particles nucleated in the gas phase and collected from the

quartz trap (see Fig. 5b). This similarity suggests a complex interplay among homogeneous and heterogeneous mechanisms of carbon formation, highlighting the challenges associated with differentiating between these types of carbon. After the formation of an amorphous carbon film on the substrate, the carbon particles previously formed in the gas phase undergo deposition and serve as additional surfaces for molecular growth (Fig. 11). In such a way, the deposition of carbon particles when already on surface influences the overall morphology of the carbon deposits. As shown in Fig. 10-zone B3, the ceramic sphere located at the end of the reactor features a carbon layer where previously deposited carbon particles likely undergo post-deposition growth. Notably, the thickness of carbon deposits varies among the investigated zones along the reactor, according to the overall gas phase maturation, similarly to what observed in the case of void reactor. Although the carbon deposits on the ceramic spheres cannot be treated as homogeneous layers due to the fluid dynamic complexities beyond the scope of this study, a qualitative variation in thickness from 0.4 to  $1.9\text{ }\mu\text{m}$  was observed between the ceramic spheres collected in Zones B1 and B3, respectively. Additionally, the carbon deposits in different zones exhibited varying structural order as evidenced by the intensity ratios of the G and D bands in the Raman spectra (Fig. 10). From Zone B2 to Zone B3, we observed an



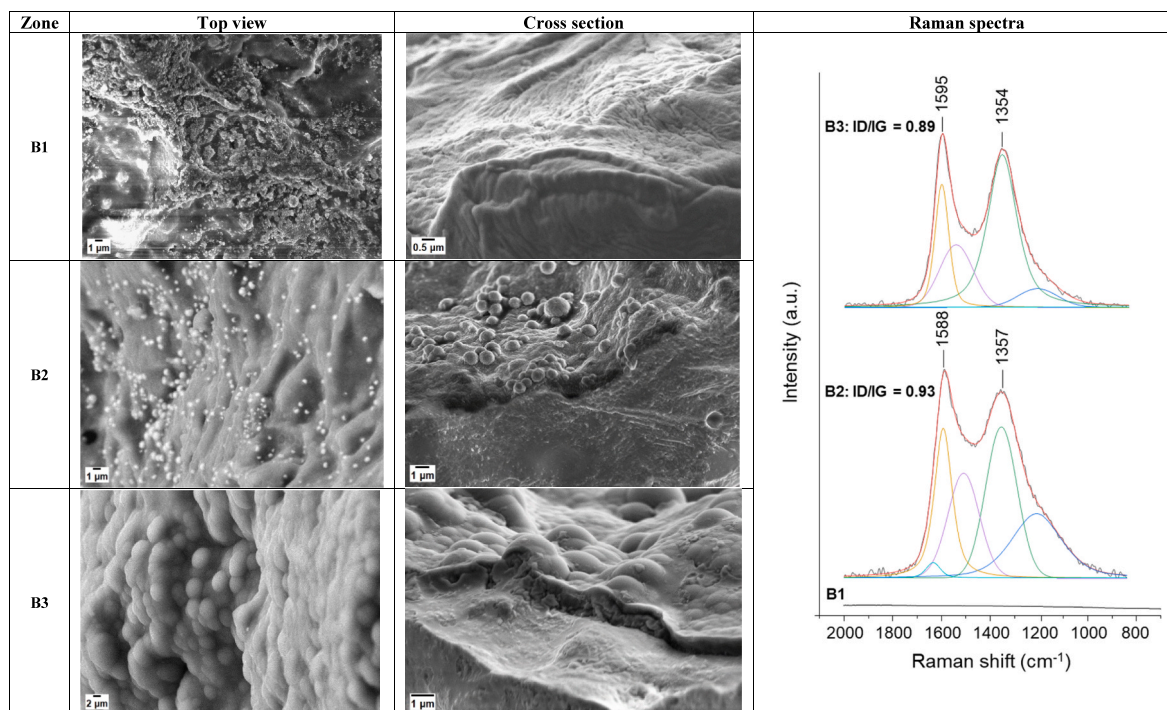


**Fig. 10.** SEM images and Raman spectra of carbon deposit on the ceramic spheres collected at the three different zones (B1: initial; B2: intermediate; B3: final)  $t_D = 30$  min,  $T = 1000$  °C.

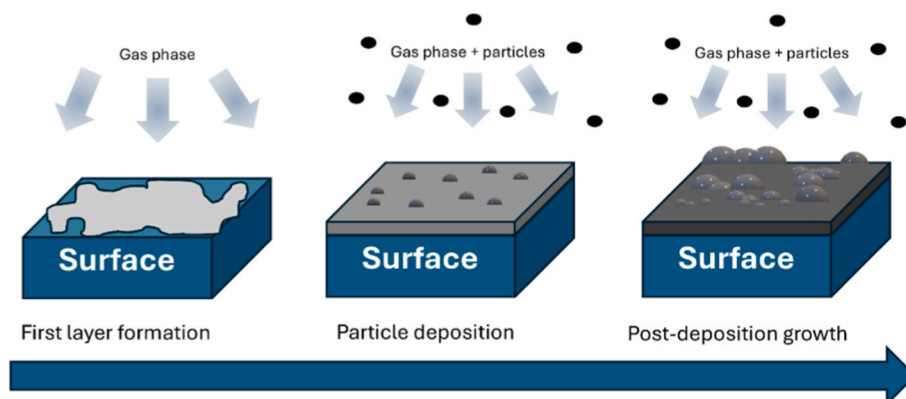


**Fig. 11.** Qualitative representation of the different steps involved in carbon deposition. 1. first layer formation; 2. particle deposition; 3. post-deposition growth.

increase in structural order, which is consistent with both the shift of the G-band peak to higher wavenumbers and the increase in the intensity of the G-band (B2: 1.27; B3: 1.54). This shift towards higher wavenumbers typically indicates enhanced crystallinity and reduced disorder in the carbon structure. Additionally, the increased intensity of the G-band

further supports the enhanced structural order and increased carbon deposit thickness in the packed reactor zone. The inhomogeneity of deposits and thick layer of carbon deposits in Zone B1 prevented collection of Raman spectra for this condition.

The effect of deposition time ( $t_D$ ) on carbon morphology at constant

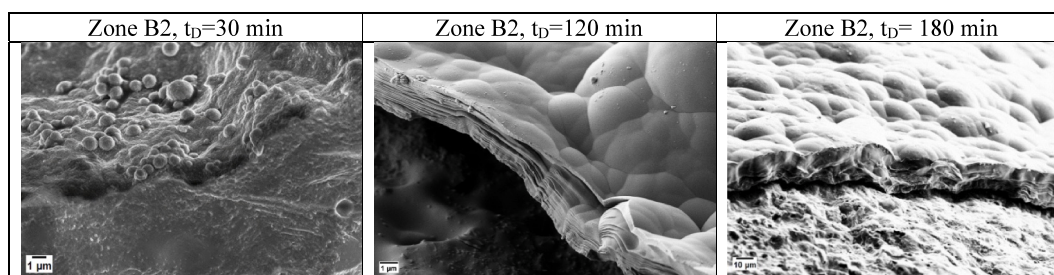


**Fig. 12.** SEM images (cross section) of carbon deposits collected at zone B2 and  $T = 1000$  °C and varying deposition times  $t_D$ . First column  $t_D = 30$  min; second column  $t_D = 120$  min; third column  $t_D = 180$  min.

temperature ( $T = 1000^\circ\text{C}$ ) and reactor position (Zone B2) is highlighted from SEM images in Fig. 12. Additional SEM images can be found in the Supplementary Material. The carbon particles embedded in the surface at  $t_D = 30$  min (left panel of Fig. 12) serve as further surfaces for layer growth which results in the morphologies observed in middle and right panels of Fig. 12 for the carbon deposits collected after  $t_D = 120$  min and  $t_D = 180$  min respectively. Once soot particles are deposited, the carbon coating will adapt to the surface's contours, enhancing the protrusions formed by the soot particles [41]. While particulate carbon tends to be isotropic, exhibiting uniformity in all directions due to its nearly spherical shape, directly deposited carbon is anisotropic, displaying directional dependence as it lacks this symmetry. Consequently, over time, as more carbon is deposited directly on the substrate rather than embedded in particles, the crystals become more aligned with the surface [42]. In addition to morphology changes, an increase in the mean thickness is observed as reported in Fig. 13. The carbon layer thickness on the ceramic spheres increases from approximately of  $1.9\ \mu\text{m}$  at  $t_D = 30$  min to  $20\ \mu\text{m}$  at  $t_D = 180$  min. It is important to note that beyond this point, carbon accumulation within the reactor makes it challenging to consistently define a carbon layer thickness. The measurements become highly variable due to factors such as gas-phase fluid dynamics around the ceramic spheres and localized soot deposition, both of which introduce significant data scattering and also different carbon morphologies (see Fig. S7).

The effect of temperature on deposited carbon morphology presented in Fig. 14 is similar to that of the position along the reactor length previously discussed. Gas phase dynamics and composition is largely influenced by temperature. At  $T = 1000^\circ\text{C}$  a more structured morphology is observed; the surface is almost entirely covered by carbon presenting big hemispherical surfaces interconnected in a layer. In fact, increasing the temperature enhances methane conversion, the concentration of gas phase species with a high C/H ratio, and the carbon growth occurring both in the gas phase and on surfaces.

Temperature and deposition time not only influence the thickness of the carbon deposits but also their structural order, both contributing to a reduction in the  $I_D/I_G$  ratio. However, between the two parameters, temperature has the most significant impact on the structural order of the deposits. As can be seen from Fig. 15a when temperature is increased from  $T = 950$  to  $T = 1000^\circ\text{C}$  the  $I_D/I_G$  ratio decreases from 0.94 to 0.75. When the deposition time is increased from 30 min to 120 min, the  $I_D/I_G$  ratio decreases from 0.89 to 0.75 (Fig. 15b). The Raman spectra further reveal that at higher temperatures and longer deposition times the G band becomes noticeably narrower, reflecting a more homogeneous

distribution of  $sp^2$  bonding and a reduction of bond-angle disorder. Narrowing of the G band is a widely recognized indicator of increasing graphitic order [43,44]. At the same time, the intensity in the region between the D and G bands—the so-called “throat”—decreases. This spectral region is known to be sensitive to interstitial defects [45] and to vibrational modes associated with amorphous carbon [46]. Therefore, the observed reduction in its intensity clearly indicates a lower amount of disordered,  $sp^3$ -rich carbon within the deposits. In line with this interpretation, the increase in deposition time leads to a progressive decrease in the overall amorphous carbon content, as previously reported for thermally driven ordering phenomena in carbon materials [47].

### 3.2. Modelling results

In this section experimental results are compared with predictions from the CRECK kinetic model describing both homogeneous pyrolysis kinetics [27] as well as carbon formation [21] and deposition [25]. Validation of the gas-phase methane pyrolysis mechanism has already been performed over a wide range of operating conditions, as reported in Ref. [19]. Aromatics, PAHs and carbon nanoparticles formation subsets have been the subject of many development and validation studies covering from pyrolysis to fuel rich flames [21,24]. To the aim of this study, we opted for the use of detailed chemistry to interpret the experimental results thus forcing the use of simple 1D configuration (see Section 2.2) despite, in the case of the packed reactor this may be inappropriate, due to residence time distribution, mixing, and possible mass transfer limitations.

Intermediate  $C_2$  species profiles ( $C_2H_4$ ,  $C_2H_2$ ,  $C_2H_6$ ) are reported as a function of methane conversion in Fig. 16, where the first row reports results for the void reactor, while the second row shows results for the packed reactor. The model captures the selectivity to the most abundant unsaturated intermediates ( $C_2H_4$ ,  $C_2H_2$ ) and underestimates selectivity to methane. The agreement between experimental results worsens in the case of the packed bed configuration, largely due to the limitation of the 1D assumption. Busillo et al. [19] previously reported comparisons of the same kinetic mechanisms with other relevant aromatics intermediates at similar conditions. As previously discussed, methyl recombination forms ethane, that dehydrogenates through a series of H-abstraction and beta-scissions to form ethylene, and acetylene. These latter are not only responsible for first aromatic ring formation, but also of surface growth at reactor walls and over ceramic surfaces. As in Serse et al. [25] the model only accounts for deposition of benzene and naphthalene within the wider set of aromatics species available in the CRECK PAH kinetic subset. As discussed in the previous sections and further proven recently in the experimental work by Selvakumar et al. [48], deposition of large PAHs and of both primary carbon nanoparticles and of aggregates is also important. Ongoing developments of the present model in this direction are outside the scope of this study and will be documented in future works.

The model can accurately reproduce total carbon formation rate in particular in the case of void reactor. Reasonable agreement is obtained also in the case of the packed reactor, with worsening agreement for increasing conversion. Numerical sensitivity analysis results illustrating the effects of varying surface-to-volume ratio and temperature on methane conversion, carbon deposit thickness, and soot volume fraction are summarized in Supplementary Material (Fig. S8). In the case of carbon deposition at the walls, or at the walls and on ceramic spheres in the case of packed reactor, the model agrees with the experimental determination with some underestimation at lower conversion in the case of void reactor (first row, Fig. 17). The model overestimates by up to 40 % carbon nanoparticles formation for the void configuration, increasing up to nearly one order of magnitude for the packed bed reactor. The missing deposition pathways of PAHs beyond naphthalene ( $C_{10}H_8$ ), including high molecular weight PAHs (BIN1-4 in the model as in Nobili et al. [28]) and of carbon nanoparticles may be responsible for

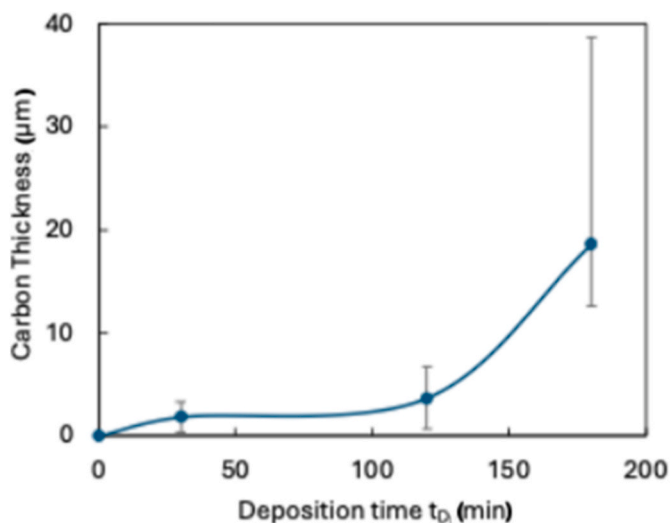


Fig. 13. Carbon thickness in Zone B2 of the packed bed reactor as a function of deposition time ( $t_D$ ) at  $T = 1000^\circ\text{C}$ .

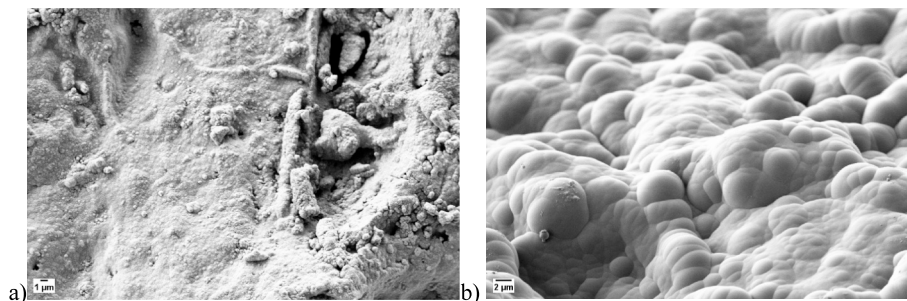


Fig. 14. SEM Images of carbon deposits after  $t_D = 120$  min at  $T = 950$  °C (a) and  $T = 1000$  °C (b) from Zone B2 of the packed reactor.

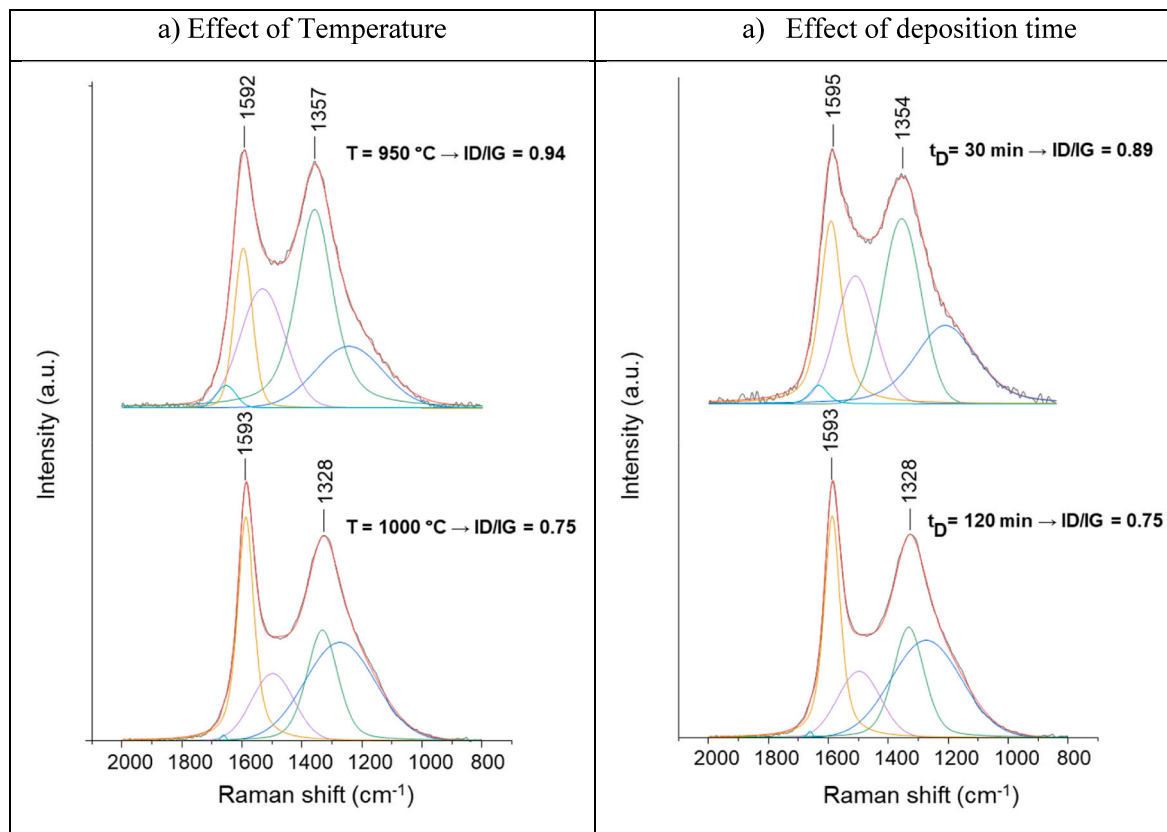


Fig. 15. Raman spectra of deposited carbon collected at different: a) temperatures (950–1000 °C), b) deposition time (30–120 min).

the large overestimation of carbon nanoparticles trapped at the reactor outlet. Further improvements of the deposition model to include deposition of large PAHs, primary particles and aggregates as implemented in the recent CRECK soot model by Nobili et al. [28] will likely lead to improved agreement.

Overall, the model captures the predominant role of deposited carbon in both cases, with an even more pronounced role of carbon deposition in the higher S/V ratio reactor configuration, i.e., the packed bed. Fig. 18 reports a comparison between collected mass of carbon. The higher amount of mass in the case of void reactor is due to the higher flow rate and thereof to a higher amount of carbon available at a given residence time. In addition, to avoid clogging and under unwanted phenomena, the deposition time in the case of the packed reactor is lower (30 min) compared to the void case (60 min). The model reproduced accurately the overall mass of produced carbon.

#### 4. Carbon nanoparticles deposition and its effect on carbon morphology

The formation of carbon deposits can occur through various mechanisms. In this context we can distinguish between two key processes: surface nucleation and surface growth [49]. Nucleation involves the condensation of planar species, such as polyaromatic structures, parallel to the substrate; growth mechanism, on the other hand, refers to the addition of reactive linear species, such as acetylene and ethylene, at the edges of graphene layers [25,30,50]. This mechanism resembles the chemical growth of soot, facilitating the expansion of carbon layers along the planes, but with the presence of substrate affecting growth directions, i.e. cone-grown formation. However, the nucleation process is not limited to molecular species; some theories also involve hydrocarbon liquid droplets or carbon particles previously formed in the gas phase [51,52]. The deposition of such particles, which is expected to be affected by their own geometry and size, can significantly influence the overall morphology of carbon deposits. In both reactor configurations



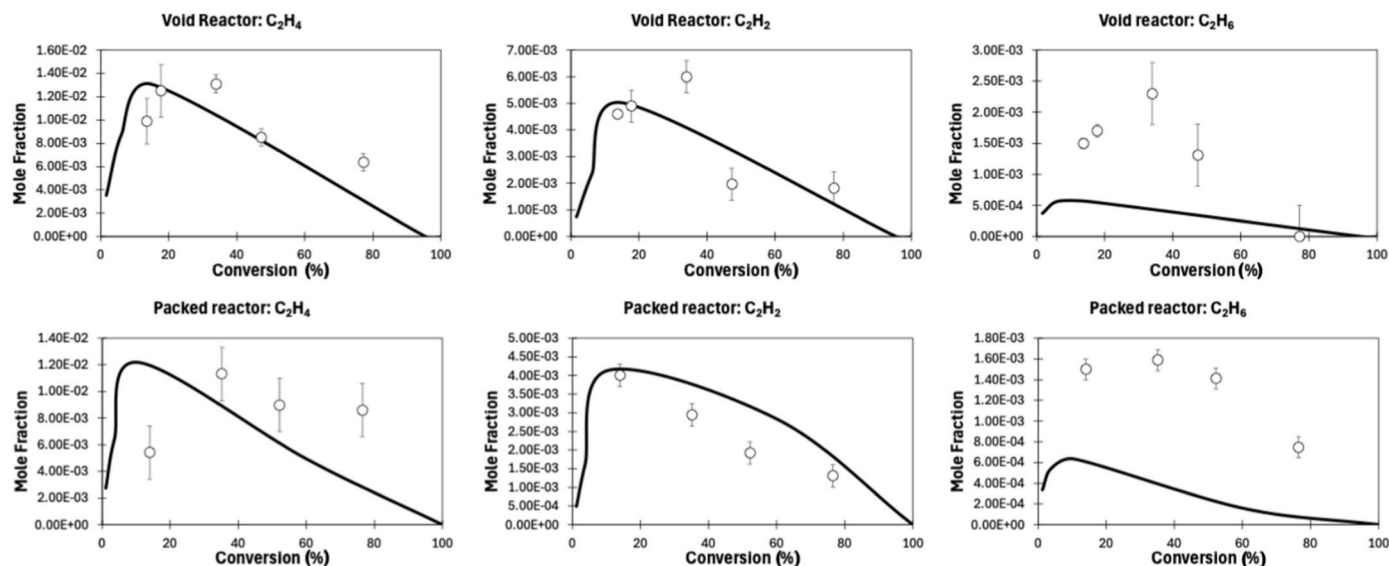


**Fig. 16.** Comparison between experimental (symbols) intermediate species profiles and model simulation results (lines) as a function of methane conversion. First row: void reactor, second row: packed reactor configuration. Error bars represent standard deviation ( $1\sigma$ ), values are reported in the attached SM together with experimental data in tabular form.

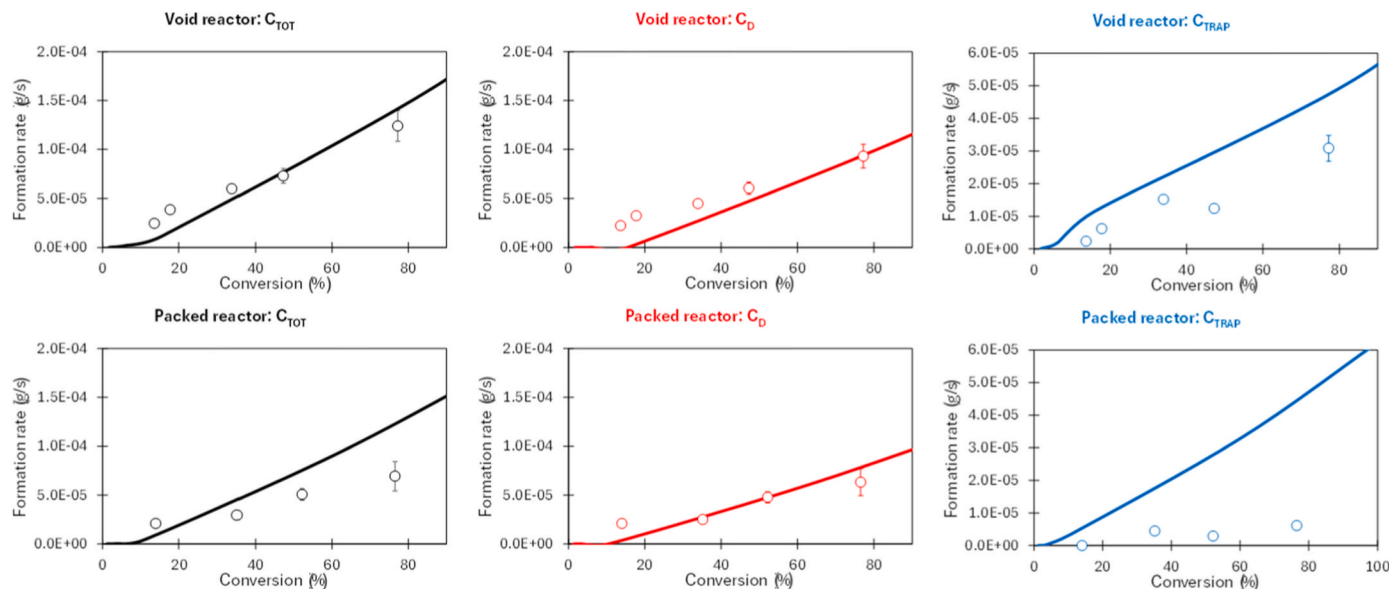


**Fig. 17.** Comparison of experimental carbon formation rates (total carbon  $C_{TOT}$ , deposited carbon  $C_D$  and carbon nanoparticles  $C_{TRAP}$ ) and model predictions as a function of methane conversion. First row: void reactor  $t_D = 60$  min. Second row: packed reactor  $t_D = 30$  min. Error bars represent standard deviation ( $1\sigma$ ), values are reported in the attached SM together with experimental data in tabular form.

(void and packed bed), cone-grown structures develop on surfaces exhibiting defects (including surface roughness and embedded gas-phase carbon particles) indicating that this morphology is a general feature of carbon deposition rather than reactor-specific. Notably, deposited carbon particles act mechanistically as surface defects, promoting cone-like structure formation analogous to that observed on mechanically roughened surfaces. The key distinction between these two nucleation pathways lies in their spatial origins: cone-like structures nucleate from pre-existing surface roughness sites in one case, but from deposited carbon particles in the other. This equivalence demonstrates that the fundamental mechanism controlling cone morphology is the availability of surface defect sites, regardless of their origin. When surface defects are present on a substrate, the cones start to grow from the substrate itself; when carbon particles undergo deposition, the cones

start at a certain height from the substrate which depends on the moment when the particle deposits. Consequently, the cones originated from gas-phase particle deposition can alter the overall structure of carbon deposits, mitigating and modifying the growth of cones due to surface defects (Fig. 19). Therefore, accurately controlling the dimensions of carbon particles (during their nucleation and growth in the gas phase) and managing their post-deposition growth, which is expected to depend also on the reactivity of the particle's surface, could be crucial for modulating morphology and optimizing carbon deposit properties. Controlling particle sizes can in fact significantly influence the kinetic of deposition and the final morphology of the pyrolytic carbon, with smaller particles leading to finer, smoother layers, and larger particles contributing to rougher deposits. As in the case of periodic protrusions, where the columns formed from higher nuclei are less



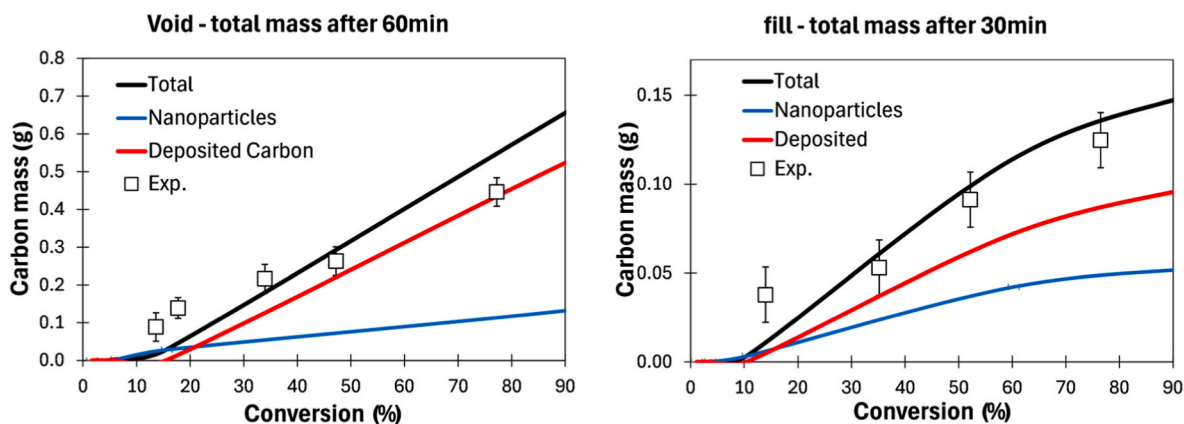


**Fig. 18.** Comparison between total carbon mass from experiments (symbols) and simulations (black lines). Specific profiles for deposited carbon (red lines) and carbon nanoparticles (blue lines) from model simulations are also reported.  $T = 1000\text{ }^{\circ}\text{C}$ , void reactor (a)  $t_D = 60\text{ min}$ , packed reactor (b)  $t_D = 30\text{ min}$ . Error bars represent standard deviation ( $1\sigma$ ), values are reported in the attached SM together with experimental data in tabular form. (For interpretation of the references to colour in this figure legend, the reader is referred to the Web version of this article.)

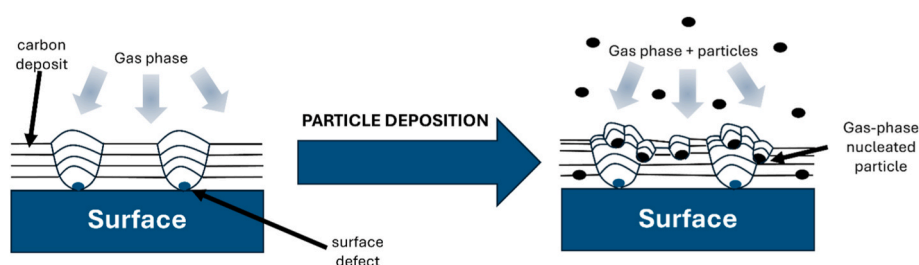


**Fig. 19.** Scheme of the effect of carbon particle deposition on the morphology of carbon deposits originating on a defective surface.

privileged than the case of single defect [53], selective carbon particles deposition may globally result in few columns and with smaller cross-sectional area, thus resembling the case of no substrate roughness. In this way by the deposition of carbon particles could be theoretically possible to compensate for any pre-existing surface protrusions.

Furthermore, establishing specific conditions for gas phase maturation, i.e. determining the optimum ratio of aromatic to small linear hydrocarbons [54], and an appropriate choice of operating temperature could turn out to be essential for the achievement of carbons with high texture.

By regulating deposition time, it is also possible to enhance surface growth while maintaining a constant size for gas-phase carbon particles. This approach could allow for further study on the effects of particles of fixed sizes on surface growth over time. In this case it is expected that deposition and final morphology would be affected by the different interactions between the surface (constantly changing over time) and fresh carbon particles with constant properties.

## 5. Conclusions

In this study, thermal methane pyrolysis was systematically investigated in a quartz tubular flow reactor to assess the influence of temperature, deposition time and surface-to-volume (S/V) ratio on carbon yield, and carbon morphology. Experimental results demonstrated that temperature plays a key role in enhancing carbon production, with overall solid carbon yields reaching up to 60 wt% at  $1150\text{ }^{\circ}\text{C}$ .

The reactor configuration strongly influenced carbon formation pathways. In the void reactor ( $S/V = 4\text{ cm}^{-1}$ ), gas-phase nucleation led predominantly to carbon nanoparticle formation, while in the packed configuration ( $S/V = 10.7\text{ cm}^{-1}$ ), the increased surface area promoted surface deposition, resulting in up to 97 % of carbon recovered as pyrolytic deposits. The carbon morphology varied significantly in the two

configurations. Surface-grown carbon evolved from thin, amorphous layers into thicker, irregular and structured films, shaped by deposition time, gas-phase composition and temperature.

SEM and Raman spectroscopy analyses revealed that increased temperature and residence time enhanced both carbon layer thickness and structural order, evidenced by decreasing  $I_D/I_G$  ratios. Gas-phase maturation and C/H ratio evolution along the reactor length were shown to modulate both the deposition rate and the structural features of carbon films. Notably, embedded carbon particles, likely nucleated in the gas phase, acted as localized nucleation centers for cone-like growth structures, confirming the complex interplay between homogeneous and heterogeneous mechanisms.

Post-deposition growth phenomena were observed to depend on both the morphology of deposited particles and the surrounding gas-phase chemistry. Reactor zone and deposition time influenced layer thickness (ranging from  $<1$  to  $>20\text{ }\mu\text{m}$ ) as well as its texture, with hemispherical features becoming more prominent downstream due to the interaction between homogeneous carbon particles and the deposit. These phenomena were linked to the continuous transformation of gas-borne species, particularly PAHs and  $\text{C}_2$  hydrocarbons, through adsorption, condensation, and growth reactions.

The CRECK kinetic model, extended with soot and surface deposition modules, effectively captured experimental trends and provided a mechanistic basis for understanding the coupling of gas-phase and surface reactions. Model simulations highlighted the importance of acetylene, aromatics and PAHs in both carbon nanoparticles formation and deposition, and the critical role of surface availability for reactor design purposes. Further improvements are urgently needed to properly model the deposition of PAHs, high molecular weight PAHs as well as carbon nanoparticles.

Overall, this study demonstrates that tuning operating parameters such as temperature, S/V ratio, and residence time can be tuned to

control both the yield and morphology of carbon formed during methane pyrolysis, enabling CO<sub>2</sub>-free hydrogen production with a valorized carbon coproduct. Depositing carbon nanoparticles on carbon deposits modifies roughness, accessible surface area, and surface chemistry, indicating opportunities for functionalization and the design of composite carbon materials with enhanced reactivity and tailored properties. These insights open pathways for applications in energy storage, catalysis and high-temperature coatings. Future work should assess scalability of this approach and examine how alternative reactor geometries and flow regimes further refine product selectivity and process performance. The combined experimental evidence and advancing kinetic modeling framework provide a foundation for multiscale reactor simulations that integrate CFD and detailed chemistry, supporting the targeted development of high-value carbon materials [51,52].

## CRediT authorship contribution statement

**Emmanuel Busillo:** Writing – original draft, Validation, Investigation, Formal analysis, Data curation. **Andrea Nobili:** Writing – review & editing, Validation, Methodology, Formal analysis. **Clarissa Giudici:** Writing – review & editing, Validation, Methodology, Formal analysis. **Maria Paola Bracciale:** Writing – review & editing, Writing – original draft, Supervision, Methodology, Investigation, Data curation. **Alberto Cuoci:** Writing – review & editing, Software, Methodology. **Paolo De Filippis:** Writing – review & editing, Supervision, Resources. **Martina Damizia:** Data curation. **Benedetta de Caprariis:** Supervision, Resources, Project administration, Funding acquisition, Formal analysis, Conceptualization. **Matteo Pelucchi:** Writing – review & editing, Supervision, Resources, Project administration, Funding acquisition, Formal analysis, Conceptualization.

## Declaration of competing interest

The authors declare the following financial interests/personal relationships which may be considered as potential competing interests: Benedetta de Caprariis reports financial support was provided by MUR ministry of research, Italy. Matteo Pelucchi reports financial support was provided by MUR ministry of research, Italy. If there are other authors, they declare that they have no known competing financial interests or personal relationships that could have appeared to influence the work reported in this paper.

## Acknowledgements

The authors gratefully acknowledge the financial support from the PRIN PNRR program of the Italian Ministry of University and Research through the project “HAMMER” P2022P7XHA and from the National Recovery and Resilience Plan (NRPP), Mission 4 Component 2 Investment 1.3-Call for tender No. 1561 of October 11, 2022 of Ministero dell'Università e della Ricerca, funded by EU-NextGenerationEU.

## Appendix A. Supplementary data

Supplementary data to this article can be found online at <https://doi.org/10.1016/j.carbon.2025.121153>.

## References

- [1] K.W. Street, K. Miyoshi, R.L. Vander Wal, Application of carbon based nano-materials to aeronautics and space lubrication, in: *Superlubricity*, Elsevier, 2007, pp. 311–340, <https://doi.org/10.1016/B978-0-444-52772-1/50050-0>.
- [2] D.S. Su, G. Centi, A perspective on carbon materials for future energy application, *J. Energy Chem.* 22 (2013) 151–173, [https://doi.org/10.1016/S2095-4956\(13\)60022-4](https://doi.org/10.1016/S2095-4956(13)60022-4).
- [3] C.-H. Kim, S.-Y. Lee, K.Y. Rhee, S.-J. Park, Carbon-based composites in biomedical applications: a comprehensive review of properties, applications, and future directions, *Adv. Compos. Hybrid Mater.* 7 (2024) 55, <https://doi.org/10.1007/s42114-024-00846-1>.
- [4] IMARC Group, Carbon black market. <https://www.imarcgroup.com/carbon-black-market> (accessed November 2025).
- [5] M. Yousefi, S. Donne, Experimental study for thermal methane cracking reaction to generate very pure hydrogen in small or medium scales by using regenerative reactor, *Front. Energy Res.* 10 (2022) 971383.
- [6] A.B. Shirsath, et al., Soot formation in methane pyrolysis reactor: modeling soot growth and particle characterization, *J. Phys. Chem. A* 127 (2023) 2136–2147.
- [7] Statista, Global carbon nanotube market value by region. <https://www.statista.com/statistics/1037740/global-carbon-nanotube-market-value-by-region/> (accessed November 2025).
- [8] N. McEvoy, N. Peltekis, S. Kumar, E. Rezvani, H. Nolan, G.P. Keeley, W.J. Blau, G. S. Duesberg, Synthesis and analysis of thin conducting pyrolytic carbon films, *Carbon* 50 (2012) 1216–1226, <https://doi.org/10.1016/j.carbon.2011.10.036>.
- [9] M. Neuwirth, T. Fleiter, P. Manz, R. Hofmann, The future potential hydrogen demand in energy-intensive industries - a site-specific approach applied to Germany, *Energy Convers. Manag.* 252 (2022) 115052, <https://doi.org/10.1016/j.enconman.2021.115052>.
- [10] BASF Report, Innovative processes for climate-smart chemistry. <https://report.basf.com/2021/en/shareholders/basf-on-the-capital-market/methane-pyrolysis.html>, 2021.
- [11] Monolith Materials/ARPA-E, Monolith Materials - Methane Pyrolysis Development, 2021.
- [12] N. Sánchez-Bastardo, R. Schlögl, H. Ruland, Methane pyrolysis for zero-emission hydrogen production: a potential bridge technology from fossil fuels to a renewable and sustainable hydrogen economy, *Ind. Eng. Chem. Res.* 60 (2021) 11855–11881, <https://doi.org/10.1021/acs.iecr.1c01679>.
- [13] W. Benzinger, K.J. Hüttinger, Chemical vapour infiltration of pyrocarbon: I. Some kinetic considerations, *Carbon* 34 (1996) 1465–1471, [https://doi.org/10.1016/S0008-6223\(96\)00117-0](https://doi.org/10.1016/S0008-6223(96)00117-0).
- [14] L. Fulcheri, et al., *Curr. Opin. Green Sustainable Chem.* 50 (2024) 100973.
- [15] A. Abánades, E. Ruiz, E.M. Ferruelo, F. Hernández, A. Cabanillas, J.M. Martínez-Val, J.A. Rubio, C. López, R. Gavela, G. Barrera, C. Rubbia, D. Salmieri, E. Rodilla, D. Gutiérrez, Experimental analysis of direct thermal methane cracking, *Int. J. Hydrogen Energy* 36 (2011) 12877–12886, <https://doi.org/10.1016/j.ijhydene.2011.07.081>.
- [16] Z. Gholami, F. Gholami, Z. Tisler, M. Vakili, A review on the production of light olefins using steam cracking of hydrocarbons, *Energies* 14 (2021) 8190, <https://doi.org/10.3390/en14238190>.
- [17] M. Yousefi, S. Donne, S. Bahremand Abrasi, M. Yousefi, Experimental study for thermal methane cracking reaction to generate very pure hydrogen in small or medium scales by using regenerative reactor, *Front. Energy Res.* 10 (2022) 986906, <https://doi.org/10.3389/fenrg.2022.986906>.
- [18] M. Mokashi, et al., Understanding of gas-phase methane pyrolysis towards hydrogen and solid carbon with detailed kinetic simulations and experiments, *Chem. Eng. J.* 479 (2024) 147556.
- [19] E. Busillo, A. Nobili, F. Serse, M.P. Bracciale, P. De Filippis, M. Pelucchi, B. de Caprariis, Turquoise hydrogen and carbon materials production from thermal methane cracking: an experimental and kinetic modelling study with focus on carbon product morphology, *Carbon* 225 (2024) 119102, <https://doi.org/10.1016/j.carbon.2024.119102>.
- [20] A. Nobili, A. Cuoci, W. Pejpichestakul, M. Pelucchi, C. Cavallotti, T. Faravelli, Modeling soot particles as stable radicals: a chemical kinetic study on formation and oxidation. Part I. Soot formation in ethylene laminar premixed and counterflow diffusion flames, *Combust. Flame* 243 (2022) 112073, <https://doi.org/10.1016/j.combustflame.2022.112073>.
- [21] A. Nobili, L. Pratali Maffei, A. Baggioni, M. Pelucchi, A. Cuoci, C. Cavallotti, T. Faravelli, On the radical behavior of large polycyclic aromatic hydrocarbons in soot formation and oxidation, *Combust. Flame* 235 (2022) 111692, <https://doi.org/10.1016/j.combustflame.2021.111692>.
- [22] G. Bagheri, E. Ranzi, M. Pelucchi, A. Parente, A. Frassoldati, T. Faravelli, Comprehensive kinetic study of combustion technologies for low environmental impact: MILD and OXY-fuel combustion of methane, *Combust. Flame* 212 (2020) 142–155, <https://doi.org/10.1016/j.combustflame.2019.10.014>.
- [23] F. Barrai, J.S. Coleman, D.A. Bhandari, F. Hershkovitz, J.R. Lattner, *Hydrocarbon Pyrolysis*, US Patent 20190161421A1, 2019.
- [24] W. Pejpichestakul, E. Ranzi, M. Pelucchi, A. Frassoldati, A. Cuoci, A. Parente, T. Faravelli, Examination of a soot model in premixed laminar flames at fuel-rich conditions, *Proc. Combust. Inst.* 37 (2019) 1013–1021, <https://doi.org/10.1016/j.proci.2018.06.104>.
- [25] F. Serse, Z. Ding, M. Bracconi, M. Maestri, A. Nobili, C. Giudici, A. Frassoldati, T. Faravelli, A. Cuoci, M. Pelucchi, A comprehensive kinetic framework for solid carbon deposition and hydrogen production from the pyrolysis of light hydrocarbons streams, *Carbon Trends* 11 (2023) 100263, <https://doi.org/10.1016/j.cartre.2023.100263>.
- [26] V.S. Arutyunov, V.I. Vedenev, *Pyrolysis of methane in the temperature range 100–1700 K*, *Russ. Chem. Rev.* 60 (1991) 1384.
- [27] E. Ranzi, A. Frassoldati, A. Stagni, M. Pelucchi, A. Cuoci, T. Faravelli, Reduced kinetic schemes of complex reaction systems: fossil and biomass-derived transportation fuels, *Int. J. Chem. Kinet.* 46 (2014) 512–542, <https://doi.org/10.1002/kin.20867>.
- [28] A. Nobili, N. Fanari, T. Dinelli, E. Cipriano, A. Cuoci, M. Pelucchi, A. Frassoldati, T. Faravelli, Kinetic modeling of carbonaceous particle morphology, polydispersity and nanostructure through the discrete sectional approach, *Combust. Flame* 269 (2024) 113697, <https://doi.org/10.1016/j.combustflame.2024.113697>.

- [29] C. Saggese, S. Ferrario, J. Camacho, A. Cuoci, A. Frassoldati, E. Ranzi, H. Wang, T. Faravelli, Kinetic modeling of particle size distribution of soot in a premixed burner-stabilized stagnation ethylene flame, *Combust. Flame* 162 (2015) 3356–3369, <https://doi.org/10.1016/j.combustflame.2015.06.002>.
- [30] R. Lacroix, R. Fournet, I. Ziegler-Devin, P.-M. Marquaire, Kinetic modeling of surface reactions involved in CVI of pyrocarbon obtained by propane pyrolysis, *Carbon* 48 (2010) 132–144, <https://doi.org/10.1016/j.carbon.2009.08.041>.
- [31] F.E. Billaud, F. Ajot, H. Micropilot plant for the study of steam-cracking feedstocks. Example of a mixture of normal paraffins, *Rev. Inst. Fr. Pét.* (1983) 763–781.
- [32] A. Cuoci, A. Frassoldati, T. Faravelli, E. Ranzi, OpenSMOKE++: an object-oriented framework for the numerical modeling of reactive systems with detailed kinetic mechanisms, *Comput. Phys. Commun.* 192 (2015) 237–264, <https://doi.org/10.1016/j.cpc.2015.02.014>.
- [33] M. Frenklach, H. Wang, Detailed modeling of soot particle nucleation and growth, *Symp. (Int.) Combust.* 23 (1991) 1559–1566, [https://doi.org/10.1016/S0082-0784\(06\)80426-1](https://doi.org/10.1016/S0082-0784(06)80426-1).
- [34] P.K. Chu, L. Li, Characterization of amorphous and nanocrystalline carbon films, *Mater. Chem. Phys.* 96 (2006) 253–277, <https://doi.org/10.1016/j.matchemphys.2005.07.048>.
- [35] S. Wang, W.J. Lee, C. Li, B. Kuan, N. Burke, J. Patel, The pyrolysis of natural gas: a study of carbon deposition and the suitability of reactor materials, *AIChE J.* 65 (2019) 1035–1046, <https://doi.org/10.1002/aic.16474>.
- [36] J.R.L.F. Coffin, Structure-property relations for pyrolytic graphite, *J. Am. Ceram. Soc.* 47 (1964) 473–478.
- [37] A. Pfrang, Y.Z. Wan, T. Schimmel, Early stages of the chemical vapor deposition of pyrolytic carbon investigated by atomic force microscopy, *Carbon* 48 (2010) 921–923, <https://doi.org/10.1016/j.carbon.2009.10.031>.
- [38] G. Paredes, T. Ondarçuhu, M. Monthieux, F. Piazza, Unveiling the existence and role of a liquid phase in a high temperature (1400 °C) pyrolytic carbon deposition process, *Carbon Trends* 5 (2021) 100117, <https://doi.org/10.1016/j.cartre.2021.100117>.
- [39] B. Reznik, K. Norinaga, D. Gerthsen, O. Deutschmann, The effect of cooling rate on hydrogen release from a pyrolytic carbon coating and its resulting morphology, *Carbon* 44 (2006) 1330–1334, <https://doi.org/10.1016/j.carbon.2005.12.014>.
- [40] J.L. Kaae, The mechanism of the deposition of pyrolytic carbons, *Carbon* 23 (1985) 665–673, [https://doi.org/10.1016/0008-6223\(85\)90226-X](https://doi.org/10.1016/0008-6223(85)90226-X).
- [41] E. López-Honorato, P.J. Meadows, P. Xiao, Fluidized bed chemical vapor deposition of pyrolytic carbon – I. Effect of deposition conditions on microstructure, *Carbon* 47 (2009) 396–410, <https://doi.org/10.1016/j.carbon.2008.10.023>.
- [42] J.L. Kaae, Microstructures of isotropic pyrolytic carbons, *Carbon* 13 (1975) 55–62, [https://doi.org/10.1016/0008-6223\(75\)90258-4](https://doi.org/10.1016/0008-6223(75)90258-4).
- [43] A.C. Ferrari, J. Robertson, Interpretation of raman spectra of disordered and amorphous carbon, *Phys. Rev. B* 61 (2000) 14095.
- [44] M.A. Pimenta, et al., Studying disorder in graphite-based systems by Raman spectroscopy, *Phys. Chem. Chem. Phys.* 9 (2007) 1276–1290.
- [45] J.N. Rouzaud, A. Oberlin, C. Beny-Bassez, Carbon films: structure and microtexture (optical and electron microscopy, Raman spectroscopy), *Thin Solid Films* 105 (1983) 75–96, [https://doi.org/10.1016/0040-6090\(83\)90333-4](https://doi.org/10.1016/0040-6090(83)90333-4).
- [46] A. Sadezky, H. Muckenhuber, H. Grothe, R. Niessner, U. Pöschl, Raman microspectroscopy of soot and related carbonaceous materials: spectral analysis and structural information, *Carbon* 43 (2005) 1731–1742, <https://doi.org/10.1016/j.carbon.2005.02.018>.
- [47] M.N. Ess, D. Ferry, E.D. Kireeva, R. Niessner, F.-X. Ouf, N.P. Ivleva, In situ Raman microspectroscopic analysis of soot samples with different organic carbon content: structural changes during heating, *Carbon* 105 (2016) 572–585, <https://doi.org/10.1016/j.carbon.2016.04.056>.
- [48] P.K. Selvakumar, F. Cepeda, F. Toth, M. Di Lorenzo, F. Farivar, T. Humphries, M. Paskevicius, M.J. Thomson, C.E. Buckley, J.W. Martin, Gas-phase origin of microwave methane pyrolysis carbon films, *Carbon* (2025) 120780, <https://doi.org/10.1016/j.carbon.2025.120780>.
- [49] Z.J. Hu, K.J. Hüttinger, Mechanisms of carbon deposition—a kinetic approach, *Carbon* 40 (2002) 624–628, [https://doi.org/10.1016/S0008-6223\(01\)00316-5](https://doi.org/10.1016/S0008-6223(01)00316-5).
- [50] C. Giudici, G. Contaldo, M. Ferri, L. Pratali Maffei, M. Bracconi, M. Pelucchi, M. Maestri, Understanding heterogeneous growth mechanisms at graphene edges: a theoretical study on acetylene deposition and mechanistic analysis, *React. Chem. Eng.* 9 (2024) 2505–2519, <https://doi.org/10.1039/D4RE00096J>.
- [51] J.C. Bokros, Variation in the crystallinity of carbons deposited in fluidized beds, *Carbon* 3 (1965) 201–211, [https://doi.org/10.1016/0008-6223\(65\)90049-7](https://doi.org/10.1016/0008-6223(65)90049-7).
- [52] R.O. Grisdale, The formation of black carbon, *J. Appl. Phys.* 24 (1953) 1082–1091, <https://doi.org/10.1063/1.1721452>.
- [53] W.J. Lee, C. Li, J. Gunning, N. Burke, J. Patel, Is the structure of anisotropic pyrolytic carbon a consequence of growth by the Volmer-Weber island growth mechanism? *Carbon* 50 (2012) 4773–4780, <https://doi.org/10.1016/j.carbon.2012.05.052>.
- [54] Z.J. Hu, W.G. Zhang, K.J. Hüttinger, B. Reznik, D. Gerthsen, Influence of pressure, temperature and surface area/volume ratio on the texture of pyrolytic carbon deposited from methane, *Carbon* 41 (2003) 749–758, [https://doi.org/10.1016/S0008-6223\(02\)00403-7](https://doi.org/10.1016/S0008-6223(02)00403-7).